Quantifying Modality Contributions via Disentangling Multimodal Representations

Padegal Amit^{1*}, Omkar Mahesh Kashyap¹, Namitha Rayasam^{1*} Nidhi Shekhar¹, Surabhi Narayan¹

¹PES University

Abstract

Quantifying modality contributions in multimodal models remains a challenge, as existing approaches conflate the notion of contribution itself. Prior work relies on accuracy-based approaches, interpreting performance drops after removing a modality as indicative of its influence. However, such outcome-driven metrics fail to distinguish whether a modality is inherently informative or whether its value arises only through interaction with other modalities. This distinction is particularly important in cross-attention architectures, where modalities influence each other's representations. In this work, we propose a framework based on Partial Information Decomposition (PID) that quantifies modality contributions by decomposing predictive information in internal embeddings into unique, redundant, and synergistic components. To enable scalable, inference-only analysis, we develop an algorithm based on the Iterative Proportional Fitting Procedure (IPFP) that computes layer and dataset-level contributions without retraining. This provides a principled, representation-level view of multimodal behavior, offering clearer and more interpretable insights than outcome-based metrics.

1 Introduction

Recent advances in multimodal learning have enabled models to process and align information across sensory modalities such as vision and language. However, despite impressive empirical results, current methods still struggle with true multimodal integration. They often exhibit modality imbalance, a tendency to over-rely on one modality while underutilizing the other Peng et al. (2022), Huang et al. (2022), Fan et al. (2023), Wei et al. (2024). As illustrated in Figure 1, this imbalance appears asymmetrically across both vision and text.

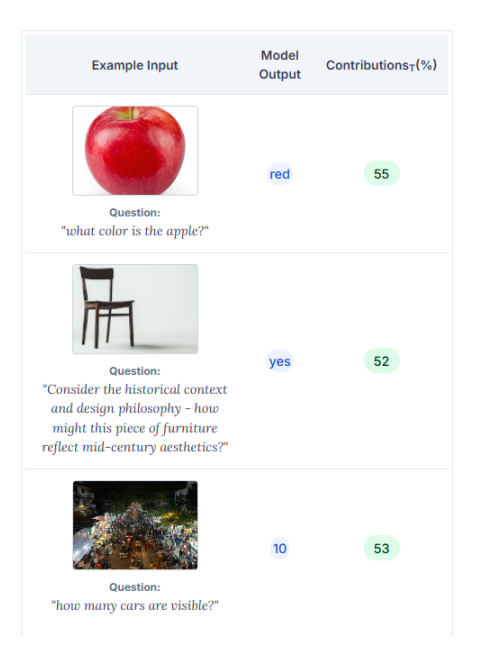


Figure 1: Overview of the proposed modality contribution framework, where text contribution (C_T) and image contribution $(C_I = 100 - C_T)$ together form a normalized 100% distribution on the BLIP model. The first row shows simple image-simple text, the second shows simple image-complex text, and the third shows complex image-simple text.

Existing works attempt to quantify modality contribution by perturbing or masking inputs (Gat et al., 2021a), (Wenderoth et al., 2025), (Wang and Wang, 2025) or by employing gradient and attention-based explanations, such as Integrated Gradients (IG) (Sundararajan et al., 2017) and Grad-CAM (Selvaraju et al., 2017). Recent works use Shapley-based approaches, such as MM-SHAP (Parcalabescu and Frank, 2022) and its extensions Wang and Wang (2025), Goldshmidt and Horovicz (2024), Goldshmidt (2025). However, these methods largely treat modalities as independent sources of information, overlooking the cross-modal interactions that emerge within the model's internal

^{*} Equal Contribution

feature space.

While the methods above often treat modalities as independent sources of information, another line of research highlights that multimodal fusion is inherently interactional. Methods such as EMAP Hessel and Lee (2020), DIME Lyu et al. (2022), and MultiViz Liang et al. (2022) demonstrate that meaningful cross-modal dependencies play a critical role in shaping the final prediction.

To bridge these perspectives, we introduce a unified information-theoretic framework that captures both modality attribution and cross-modal interactions through PID (Williams and Beer, 2010). PID decomposes total predictive information into unique, redundant, and synergistic components. This principled decomposition offers clear insights into how individual modalities contribute both independently and collectively, enabling a deeper understanding of how multimodal fusion arises within the model's internal feature representations.

Unlike previous PID-based approaches that rely on computationally intensive conic solvers or require auxiliary network training (Liang et al., 2023), we present a scalable, inference-only approximation leveraging the Iterative Proportional Fitting Procedure (IPFP) (Bacharach, 1965). This makes our approach parameter-free, computationally efficient, and directly applicable for post-hoc multimodal analysis.

Our key contributions are as follows:

- We propose the first modality contribution metric that jointly captures modality-specific and interactional effects.
- We develop a quantification approach based on PID and propose a novel, computationally efficient metric derived using the IPFP algorithm.
- We evaluate our method across diverse VLMs and datasets, supported by synthetic experiments and ablation studies.

2 Related work

2.1 Gradient and Attention-Based Methods

Gradient-based approaches, such as Integrated Gradients (IG) Sundararajan et al. (2017) attribute contributions through path-integrated gradients but suffer from instability, baseline sensitivity, and high attribution noise (Zhuo and Ge, 2024). By relying

solely on explicand gradients and neglecting counterfactual ones, IG fails to capture higher-order effects, like redundant or synergistic contributions, where features jointly influence predictions in non-additive ways, and violates key Shapley axioms, yielding spurious attributions. More broadly, gradient saliency often reflects the model's implicit density induced by the softmax layer rather than genuine discriminative reasoning (Srinivas and Fleuret, 2020).

Attention-based explanations share similar pit-falls. Attention weights may misrepresent causal polarity (Liu et al., 2022), fail to correlate with true feature importance (Wiegreffe and Pinter, 2019), and can be adversarially altered without affecting predictions (Serrano and Smith, 2019). White-box visualization methods such as attention maps and Grad-CAM Selvaraju et al. (2017) offer coarse interpretability but remain architecture-dependent and cannot disentangle synergistic from suppressive cross-modal effects.

2.2 Perturbation-based methods

Early studies on quantifying modality contribution focused on uncovering dataset biases that enable strong unimodal performance (Goyal et al., 2017a). Subsequent work introduced perturbation-based tests to quantify modality importance by observing performance degradation when one modality is removed or altered. These approaches fall into two categories: deletion methods, which suppress or mask modality features (Shekhar et al., 2017a; Madhyastha et al., 2018; Frank et al., 2021), and contradiction or foiling methods, which inject misleading inputs such as swapped captions or textual foils (Gat et al., 2021b; Shekhar et al., 2019; Parcalabescu et al., 2022). However, their reliance on accuracy-based evaluation limits interpretability, as accuracy of the models outweighs genuine crossmodal understanding. This dependence has led to inconsistent findings across studies and highlights the need for performance-agnostic approaches that more reliably capture true modality reliance.

2.3 Shapley-based methods

Shapley-based methods, grounded in Shapley theory (Shapley et al., 1953), provide a principled framework for attributing model predictions by averaging each feature's marginal contribution over all possible subsets of features (Lundberg and Lee, 2017). TokenSHAP Goldshmidt and Horovicz (2024) and PixelSHAP Goldshmidt (2025) extend

this framework to tokens and image regions, respectively, yielding fine-grained unimodal attributions but missing cross-modal dependencies. Multi-SHAP (Wang and Wang, 2025) models patch-token interactions to separate synergistic and suppressive effects, but it incurs high Monte Carlo cost. MM-SHAP (Parcalabescu and Frank, 2022) introduces a performance-agnostic metric that aggregates absolute Shapley contributions per modality, however it captures only aggregate modality proportions, discarding directional and interaction information and remaining sensitive to masking artifacts.

3 Methodology

PID extends classical information theory to multiple sources by decomposing the total mutual information $I_p(X_1, X_2; Y)$, where X_1, X_2 , and Y represent the distributions of two sources and the target variable, respectively, into four distinct components:

 Redundant Information (R): Information about Y that is shared by both sources X₁ and X₂:

$$R = \max_{q \in \Delta_p} I_q(X_1; X_2; Y) \tag{1}$$

• Unique Information from Source 1 (U_1) : The information about Y provided exclusively by source X_1 , without overlap from source X_2 :

$$U_1 = \min_{q \in \Delta_n} I_q(X_1; Y \mid X_2) \tag{2}$$

• Unique Information from Source 2 (U_2) : The information about Y provided exclusively by source X_2 , without overlap from source X_1 :

$$U_2 = \min_{q \in \Delta_p} I_q(X_2; Y \mid X_1), \tag{3}$$

(4)

• **Synergistic Information** (S): The information that arises only when both sources X_1 and X_2 are considered jointly, capturing their interaction:

$$S = I_p(X_1, X_2; Y) - \min_{q \in \Delta_p} I_q(X_1, X_2; Y)$$

These four components satisfy the fundamental decomposition:

$$I_n(X_1, X_2; Y) = R + U_1 + U_2 + S$$

This decomposition explicitly disentangles individual modality contributions (U_1, U_2) from cross-modal interactions (R, S). Together, these components provide a principled way to disentangle modality-specific and joint information contributions within multimodal fusion.

3.1 Computing PID

Let $X_1 \in \mathcal{X}_1$ and $X_2 \in \mathcal{X}_2$ denote the text and image embeddings, respectively, and $Y \in \mathcal{Y}$ represent the output embeddings. Define the simplex of all joint distributions,

$$\Delta = \mathcal{P}(X_1 \times X_2 \times Y)$$

and the affine feasible set.

$$\Delta_p = \left\{ q \in \Delta : q(x_i, y) = p(x_i, y), \\ \forall x_i \in \mathcal{X}_i, \ y \in \mathcal{Y}, \ i \in \{1, 2\} \right\}$$
(5)

which preserves the observed modality-target marginals $p(x_1, y)$ and $p(x_2, y)$.

Following Liang et al. (2023), the PID components are obtained via a KL-projection formulation:

$$H_{q}(Y \mid X_{1}, X_{2}) = \log |\mathcal{Y}| - \text{KL}(q \parallel \tilde{q}),$$
where $\tilde{q}(x_{1}, x_{2}, y) = \frac{q(x_{1}, x_{2})}{|\mathcal{Y}|}$ (6)

Here, the joint distribution $q(x_1, x_2, y)$ can be represented as a tensor Q of shape $|X_1| \times |X_2| \times |\mathcal{Y}|$. However, optimizing over the full joint tensor Q is computationally expensive. We discuss this in more detail in Appendix 8

To address this, we first consider the corresponding convex problem that solves Equation (6).

$$\arg\min_{Q,\tilde{Q}} F(Q,\tilde{Q}) = \text{KL}(Q \| \tilde{Q})$$
s.t. $\tilde{Q}(x_1, x_2, y) = \frac{Q(x_1, x_2)}{|\mathcal{Y}|} \quad \forall x_1, x_2, y,$

$$\sum_{x_2} Q(x_1, x_2, y) = p(x_1, y), \quad \forall x_1, y,$$

$$\sum_{x_1} Q(x_1, x_2, y) = p(x_2, y), \quad \forall x_2, y,$$

$$Q \ge 0, \quad \forall x_1, x_2, y,$$

$$\sum_{x_1, x_2, y} Q(x_1, x_2, y) = 1.$$
(7)

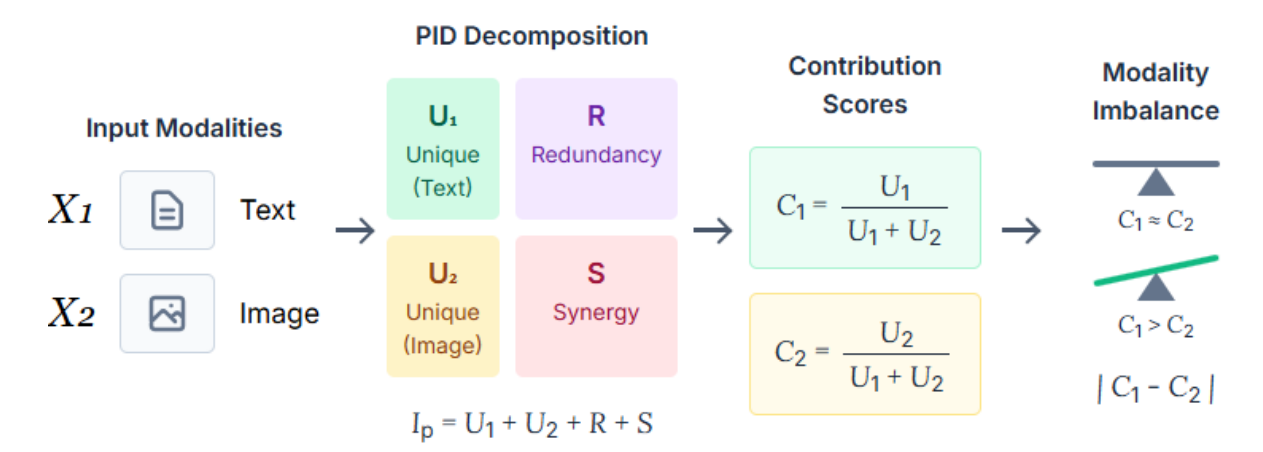


Figure 2: Overview of the proposed modality contribution framework, where text contribution (C_T) and image contribution ($C_I = 100 - C_T$) together form a normalized 100% distribution.

The objective $F(Q, \tilde{Q})$ is jointly convex in both arguments, and all constraints are affine. Hence, Equation (7) defines a well-posed convex program over the positive orthant.

Theorem 1 (Existence and Uniqueness of Q^*). The subproblem in Equation 7

$$Q^{\star} = \arg\min_{Q \in \Delta_{p}} \mathrm{KL}(Q \parallel \tilde{Q})$$

admits a unique minimizer $Q^* \in \Delta_p$.

Proof. Under the assumptions outlined in Appendix 8, the set Δ_p is compact and convex, which guarantees that the KL projection is both well-defined and unique. This justifies the use of the I-projection results from Csiszár et al. (2004), which we leverage to prove the theorems. These results are further detailed in Appendix 3.

Thus, Theorem 3 establishes that our formulation yields the same optimizer as that of Liang et al. (2023), ensuring consistency with prior work.

3.2 Alternating Minimization via IPFP

We solve Equation (7) by alternating KL-projections, following the structure of IPFP. At each iteration t, we update Q and \tilde{Q} as follows.

(1) **Q-step (I-projection).** Given the current iterate $\tilde{Q}^{(t)}$, update:

$$Q^{(t+1)} = \arg\min_{Q \in \Delta_n} \mathrm{KL}(Q \parallel \tilde{Q}^{(t)}).$$

This projection enforces the marginal constraints $p(x_1, y)$ and $p(x_2, y)$ while staying closest to $\tilde{Q}^{(t)}$ under the KL divergence. Since the constraints in

 Δ_p factorize over labels y, the problem decomposes into independent subproblems

$$Q_y^{(t+1)} = \arg\min_{Q_y \in \Delta_{p(y)}} \operatorname{KL}(Q_y \parallel \tilde{Q}_y^{(t)}),$$

each corresponding to a label-specific KL-regularized optimal transport problem. Each of these can be efficiently solved using Sinkhorn iterations (Cuturi, 2013).

(2) \tilde{Q} -step (closed-form update). Given the updated coupling $Q^{(t+1)}$, the auxiliary variable is updated as

$$\tilde{Q}^{(t+1)}(x_1, x_2, y) = \frac{Q^{(t+1)}(x_1, x_2)}{|\mathcal{Y}|},$$

which is the closed-form solution minimizing $\mathrm{KL}(Q^{(t+1)} \parallel \tilde{Q})$ under the normalization constraint. This alternation monotonically decreases $F(Q,\tilde{Q})$ and converges globally.

Theorem 2 (Global convergence of alternating KL-projections). Let $(Q^{(t)}, \tilde{Q}^{(t)})$ be the iterates produced by the alternating minimization (See Section 7). Define $F(Q, \tilde{Q}) := \mathrm{KL}(Q \parallel \tilde{Q})$. Then

$$F(Q^{(t+1)}, \tilde{Q}^{(t+1)}) \leq F(Q^{(t)}, \tilde{Q}^{(t)}) \quad \forall t,$$

and the sequence $\{F(Q^{(t)}, \tilde{Q}^{(t)})\}$ converges monotonically to a unique global minimum $F^* \geq 0$. Moreover, $Q^{(t)} \to Q^*$, where Q^* is the unique minimizer of Equation (7) and $\tilde{Q}(t) \to \tilde{Q}^*$, the corresponding projection of \tilde{Q} onto $Q_y \in \Delta_p(y)$

Proof. The result follows from the alternating divergence minimization theorem of (Csiszár et al., 2004), applied to the two convex sets defined by

the Q-step and \tilde{Q} -step projections. Monotonic decrease follows from the three-point property of KL divergence, and convergence from compactness and strict convexity of the KL divergence. A detailed proof is provided in Appendix 8. \Box

Thus, Theorem 2 guarantees that the alternating I-projection procedure is globally convergent and initialization-independent, with each iteration strictly decreasing the objective until reaching the fixed point Q^* .

Direct IPFP (Sinkhorn) updates may suffer from numerical instability due to repeated exponentiation and multiplication of small values. Following Peyré et al. (2019), we perform all updates in the log domain for stability. For each label $y \in Y$, define the positive kernel $A_y(x_1, x_2) = \tilde{Q}(x_1, x_2, y) > 0$ and marginals $r_y(x_1) = p(x_1, y)$, $c_y(x_2) = p(x_2, y)$.

The stabilized Sinkhorn updates are:

$$\log u_y \leftarrow \log r_y - LSE_{x_2} (\log A_y + \log v_y),$$

$$\log v_y \leftarrow \log c_y - LSE_{x_1} (\log A_y + \log u_y),$$

where $LSE(\cdot)$ denotes the log-sum-exp operator, ensuring numerical stability. After convergence,

$$R_y = \exp(\log A_y + \log u_y + \log v_y)$$

= diag(u_y) A_y diag(v_y), (9)

which satisfies the marginal constraints exactly. We also include the Algorithm of our IPFP approach in Appendix 8.

3.3 Modality Contribution Metric

Having obtained scalable estimates of the PID components via our IPFP-based solver, we now construct interpretable modality contribution metrics that directly quantify how much each modality contributes to model predictions.

We define the normalized contribution of modality i as

$$C_i = \frac{U_i}{\sum_j U_j},\tag{10}$$

where U_i is the unique information provided by modality i. The sum in the denominator normalizes the contributions, ensuring they are expressed as fractions of the total unique information across all modalities. This normalization allows C_i to represent the relative importance of each modality, independent of the absolute scale of unique information, and ensures that the contributions sum to 1. We explain the complete framework in Figure 2.

3.4 Why PID enables a contribution score

By isolating the unique information (U_1, U_2) from both shared and synergistic effects, PID provides a clear distinction between information contributed independently by each modality and that which emerges from cross-modal interactions. This separation helps prevent conflating individual and interactional contributions. Importantly, PID is accuracy-agnostic, meaning it quantifies information content regardless of whether the model's predictions are correct (Parcalabescu and Frank, 2022). Recent work has also emphasized the limitations of perturbation-based methods, advocating for approaches that analyze a model's internal representations rather than relying solely on its outputs (Sim et al., 2025). PID naturally aligns with this perspective, as it operates directly on the model's internal feature distributions. This allows for the computation of modality contribution scores while capturing cross-modal dynamics, without requiring model perturbations.

4 Implementation Details

Following Liang et al. (2023), we estimate PID by first converting the continuous modality embeddings into discrete distributions with finite support. To do this, we apply feature binning and clustering techniques. Specifically, for high-dimensional embeddings, we use K-means clustering to obtain discrete support sets $|X_1|$, $|X_2|$ and Y for the two modalities and the target.

The IPFP solver runs for up to 50 iterations. Within each iteration, it performs a maximum of 100 Sinkhorn updates in the log domain (see Equation 8) per label. The iterative process halts early if either the marginal deviation or the relative change in the KL objective $F(Q,\tilde{Q})$ drops below a threshold of 1×10^{-8} .

5 Experiments

5.1 Synthetic dataset

Our first goal is to evaluate the accuracy of our proposed estimators with respect to the ground truth or human judgment, as done by Liang et al. (2023). We sample from a binary bitwise distribution where each bitwise operator's PID can be solved exactly when y and x_i 's are discrete and low-dimensional.

The and dataset $(y = x_1 \land x_2)$ exhibits moderate synergy, as the output is 1 only when both inputs are 1, requiring joint information. It has

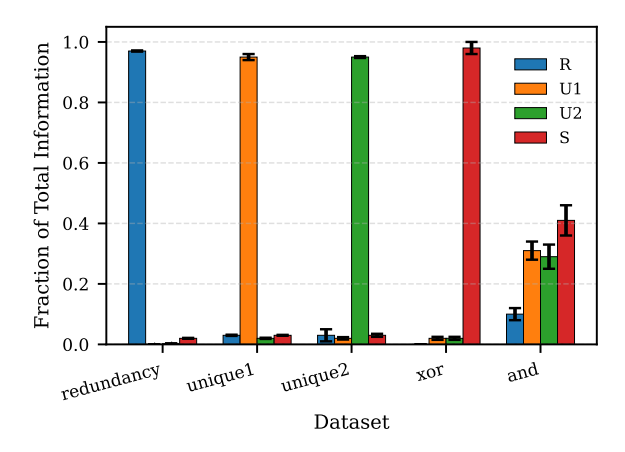


Figure 3: Comparison of proposed estimators with true PID values on synthetic datasets based on binary bitwise operations. R = Redundancy, U1 & U2 = Unique information, S = Synergy.

little redundancy since neither input alone reliably predicts y=1, but some unique information is present because if either input is 0, the output is 0.

In the *xor* dataset $(y = x_1 \oplus x_2)$, synergy is high because neither input alone predicts y, and there is no redundancy or unique information in the individual inputs; only their combination reveals the output. The *unique1* dataset $(y = x_1)$ contains no synergy or redundancy because x_2 adds no information, and all information about y is unique to x_1 . The unique2 dataset $(y = x_2)$ mirrors unique1, but with the roles of the inputs reversed: all information about y is uniquely provided by x_2 , while x_1 contributes nothing. As such, it contains no redundancy or synergy. Lastly, the redundancy dataset, where both inputs are identical (x_1, x_1) and $y = x_1$, has no synergy but maximum redundancy since both predictors share the same information about y. Figure 3 illustrates that our estimated PID components are consistent with the theoretical characteristics of these synthetic datasets, providing evidence of the estimator's validity.

5.2 Synthetic Validation of Fusion Mechanisms

To verify that the proposed metric behaves as expected under controlled conditions, we conduct a synthetic validation experiment using two independent Gaussian variables: $X_1 \sim \mathcal{N}(0,1)$ and $X_2 \sim \mathcal{N}(0,1)$ To ensure statistical independence, the inputs are decorrelated using Independent Component Analysis (ICA) (Hyvärinen et al., 2001). The synthetic output Y is generated under several predefined fusion rules: $add(Y = X_1 + X_2)$, mul

 $(Y = X_1 \times X_2)$, weighted 10 $(Y = X_1 + 10X_2)$, weighted $100(Y = X_1 + 100X_2)$ and only one in $put(Y = X_2)$. These formulations emulate different multimodal interactions, from balanced contributions to strongly biased or multiplicative relationships. Because the ground-truth modality contributions are analytically known, this setup provides a reliable way to validate the metric's correctness. As expected, additive and multiplicative fusion produce approximately equal contributions from both modalities (around 50%), while weighted fusion shifts the contributions toward the modality with the larger coefficient, as shown in Figure 4. These results confirm that the proposed metric reliably captures true modality influence and accurately reflects the underlying fusion dynamics rather than random variation.

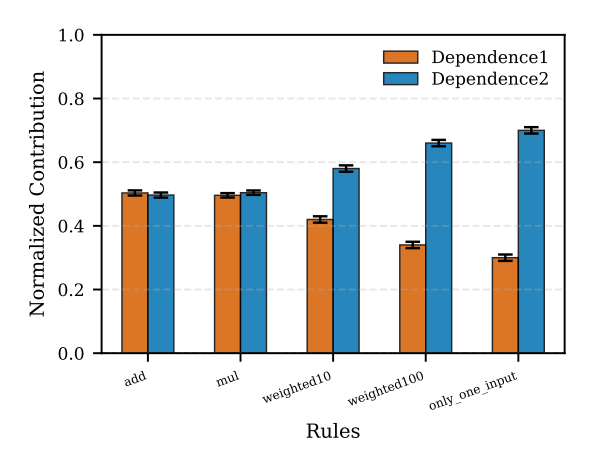


Figure 4: Synthetic validation of the proposed PID-based metric based on rules: additive, multiplicative, weighted additive and single input.

5.2.1 Experimental Setup

We apply our method on pretrained models without any further training. For each model, we extract the relevant intermediate representations and compute the PID decomposition, yielding per-sample contributions from each modality. This approach enables comparison of modality contributions across different tasks, ensuring the results reflect true model behavior rather than dataset-specific biases or random fluctuations (Parcalabescu and Frank, 2022).

5.2.2 Models

We evaluate our metric across models that differ in both fusion strategy and model scale. Specifically, we consider two primary fusion paradigms: (1) cross-attention-based fusion, which enables dynamic interaction between modalities,

Model	VQA		GQA		COCO			ScienceQA		NLVR2		
	Text	Image	Text	Image	Ori	ginal	FOIL-COCO		Text	Image	Text	Image
					Text	Image	Text	Image				
PaliGemma2-3B	53.60	46.39	56.44	43.55	55.10	44.90	54.80	45.20	53.29	46.70	48.63	51.36
SmolVLM-500M	60.90	39.10	58.30	41.60	59.80	40.10	60.10	39.80	53.30	46.60	65.18	34.81
LLaVA-1.5-7B	59.16	40.84	57.90	42.10	58.50	41.50	58.70	41.30	54.20	45.80	52.40	47.60
BLIP	55.45	44.55	54.58	45.42	58.94	41.05	57.32	42.68	52.90	47.10	53.80	46.10

Table 1: Modality-specific score (%) of various models across multiple benchmarks. The COCO dataset is subdivided into Original and FOIL-COCO settings (Shekhar et al., 2017b), each reporting results with text-only and image-only input.

and (2) concatenation-based fusion, which combines modality embeddings in a shared feature space without explicit cross-modal exchange. BLIP (Li et al., 2022), a relatively compact 3Bparameter model, exemplifies the cross-attention approach through its Query Transformer (Q-Former), which bridges frozen image and text encoders via lightweight query-based attention for fine-grained alignment. In contrast, LLaVA-1.5 (Liu et al., 2023), a larger 7-B parameter model, and PaliGemma2 (Steiner et al., 2024), also with 3B parameters, employ concatenation-based fusion within their architectures. SmolVLM (Marafioti et al., 2025), with 500M parameters, serves as an efficiency-oriented variant of the same paradigm. This range, from different fusion paradigms to different model sizes, allows us to examine how fusion mechanisms and model capacity jointly influence modality contributions and cross-modal interactions. All models were evaluated using 4-bit quantization to reduce memory footprint and computational cost while maintaining performance.

5.2.3 Tasks and Datasets

We evaluate our metric on five multimodal benchmarks covering diverse modality dependencies. VQA (Goyal et al., 2017b) and GQA (Hudson and Manning, 2019) represent balanced multimodal tasks that require joint visual-textual reasoning, making them ideal for testing whether our metric captures equal modality influence. NLVR2 (Suhr et al., 2018) focuses on visual reasoning, where models must determine whether textual descriptions align with paired images, providing a setting to evaluate cross-modal grounding and potential visual dominance. ScienceQA (Saikh et al., 2022) features variable modality reliance, as different question types depend more heavily on either text or visuals, allowing us to assess sensitivity to task-specific modality shifts. Finally, FOIL-COCO (Shekhar et al., 2017b) introduces controlled textual discrepancies, testing whether the metric can detect how subtle linguistic perturbations alter modality contributions.

5.2.4 Results

Across VQA and GQA, all major models like BLIP, LLaVA, and PaliGemma show consistent modality attributions, with text contributing around 55% and image 45%, indicating a balanced integration of linguistic and visual information (Table 1). This alignment across architectures confirms that our metric captures a stable and interpretable modality balance, consistent with prior findings that both datasets encourage joint reasoning over text and image content. SmolVLM, however, exhibits a slightly higher text bias (60%), likely reflecting its smaller capacity and lighter visual backbone. The near-equal contributions observed for larger models can also be attributed to their VQA-style training objectives, which emphasize textual regularities while maintaining visual grounding (Goyal et al., 2017a). Overall, these results validate that balanced benchmarks like VQA and GQA yield moderate, near-equal modality contributions when analyzed through our information-theoretic framework.

On ScienceQA, modality contributions show greater variability, with text slightly dominating ($\approx 53\text{-}55\%$) due to the dataset's heterogeneous question types. BLIP and SmolVLM exhibit more balanced behavior, indicating better adaptation to visual reasoning, whereas LLaVA and PaliGemma remain more text-oriented.

For NLVR2, a visually grounded reasoning task, most models exhibit an increase in image contribution, consistent with its emphasis on spatial and relational understanding. However, SmolVLM remains notably text-oriented ($\approx 65\%$ text vs. 35% image), suggesting limited visual grounding likely due to its smaller capacity and lightweight

visual encoder. In contrast, BLIP, LLaVA, and PaliGemma demonstrate a more balanced distribution between modalities, aligning with their larger architectures and more expressive fusion mechanisms.

On the FOIL-COCO dataset, we note that the modality contribution scores do not deviate significantly from the baseline, indicating that minor textual perturbations do not drastically alter the model's overall modality balance. This behavior is consistent with observations from (Parcalabescu and Frank, 2022), which similarly reported stability under subtle input modifications. Among models, PaliGemma continues to show relatively lower text contribution, while SmolVLM exhibits a stronger bias toward text, reinforcing trends observed in other benchmarks.

6 Ablation

6.1 Fusion Method Ablation

We evaluated the impact of different multimodal fusion strategies on modality contributions. Table 2 presents the average contributions of image and text for four fusion methods: $Img \rightarrow Text$ (cross-attention from image to text, where the image guides the processing of text), $Txt \rightarrow Image$ (cross-attention from text to image, where the text guides the processing of the image), Concatenation (which combines image and text features into a single representation vector without direct interaction), and $Bidirectional\ Fusion$ (where the model simultaneously attends to both modalities, allowing mutual influence).

Fusion	Image	Text
$Img \rightarrow Txt$	55.3	44.7
$Txt \rightarrow Img$	38.5	61.5
Concatenation	45.6	54.4
Bidirectional Fusion	54.7	45.3

Table 2: Ablation study comparing different multimodal fusion methods and their impact on modality contributions.

From the results, we observe that the direction of cross-attention significantly affects the balance of modality contributions. Specifically, $Img \rightarrow Text$ slightly favors the image (55.3%), while $Txt \rightarrow Img$ overemphasizes the text (61.5%), potentially underestimating image's contribution. In contrast, *Concatenation* and *Bidirectional Fusion* achieve

a more balanced distribution, indicating a stable and equitable utilization of both modalities. These findings suggest that symmetric fusion methods, like concatenation and bi-directional fusion, may be preferable in scenarios where both modalities are expected to contribute equally, and that text to image cross-attention may introduce systematic bias toward text.

6.2 Modality perturbations

To further investigate the sensitivity of the model to modality-specific perturbations, we conducted an ablation by varying the textual and image input. We examined two forms of text corruption: (1) randomly shuffling word order and (2) replacing text with dummy content (Lorem Ipsum). For the image input, we applied Gaussian noise to it. Table 3 summarizes the mean image and text contributions for each condition.

Perturbation	Image	Text		
Original	42.6	57.4		
Noisy image	44.9	55.1		
Dummy text	47.7	52.3		
Jumbled text	38.8	61.2		

Table 3: Ablation study showing the mean of image and text contributions under different input perturbations.

The results show that perturbations consistently shift modality contributions. Adding noise to the images slightly increases image dependence, indicating the model adapts to the altered input. Replacing the text with dummy content or jumbling the word order increases text reliance, reflecting the model's sensitivity to disruptions in the linguistic signal. Notably, the increase in text contribution for jumbled inputs underscores the role of positional encoding in maintaining semantic structure.

7 Conclusion

We present a principled framework for quantifying modality contributions in multimodal models using PID. Our method operates directly on internal representations, enabling the separation of unique, redundant, and synergistic information, and distinguishing inherent modality importance from cross-modal interactions. Through validation on synthetic data, diverse benchmarks, and models such as BLIP, LLaVA, PaliGemma, and SmolVLM, we demonstrate that our metric produces consis-

tent, interpretable patterns that align with known dataset biases. These results establish our approach as a scalable, model-agnostic, and performance-independent tool for analyzing multimodal interactions.

8 Limitations

While our PID-based framework provides a principled lens for analyzing modality contributions, it is not without limitations. First, the PID estimates are sensitive to noise in the embedding space, as small variations in feature distributions can influence the inferred information components. Second, as with other recent analyses, the method may not be fully immune to spurious correlations in the data or model representations, which could affect the attribution scores. Finally, the approach assumes access to intermediate model embeddings, which may not always be available for closed-source or APIrestricted systems. Addressing these challenges, particularly improving robustness to noise and mitigating the influence of spurious correlations, remains an important direction for future work.

References

- Michael Bacharach. 1965. Estimating nonnegative matrices from marginal data. *International Economic Review*, 6(3):294–310.
- Thomas M Cover. 1999. *Elements of information theory*. John Wiley & Sons.
- Imre Csiszár. 1984. Information geometry and alternating minimization procedures. Statistics and Decisions, Dedewicz, 1:205–237.
- Imre Csiszár, Paul C Shields, et al. 2004. Information theory and statistics: A tutorial. *Foundations and Trends® in Communications and Information Theory*, 1(4):417–528.
- Marco Cuturi. 2013. Sinkhorn distances: Lightspeed computation of optimal transport. *Advances in neural information processing systems*, 26.
- Yunfeng Fan, Wenchao Xu, Haozhao Wang, Junxiao Wang, and Song Guo. 2023. Pmr: Prototypical modal rebalance for multimodal learning. In *Proceedings of the IEEE/CVF Conference on Computer Vision and Pattern Recognition*, pages 20029–20038.
- Stella Frank, Emanuele Bugliarello, and Desmond Elliott. 2021. Vision-and-language or vision-for-language? on cross-modal influence in multimodal transformers. In *Proceedings of the 2021 Conference*

- on Empirical Methods in Natural Language Processing, pages 9847–9857, Online and Punta Cana, Dominican Republic. Association for Computational Linguistics.
- Itai Gat, Idan Schwartz, and Alex Schwing. 2021a. Perceptual score: What data modalities does your model perceive? *Advances in Neural Information Processing Systems*, 34:21630–21643.
- Itai Gat, Idan Schwartz, and Alexander Schwing. 2021b. Perceptual score: What data modalities does your model perceive?
- Roni Goldshmidt. 2025. Attention, please! pixelshap reveals what vision-language models actually focus on. *ArXiv*, abs/2503.06670.
- Roni Goldshmidt and Miriam Horovicz. 2024. Tokenshap: Interpreting large language models with monte carlo shapley value estimation.
- Yash Goyal, Tejas Khot, Douglas Summers-Stay, Dhruv Batra, and Devi Parikh. 2017a. Making the v in vqa matter: Elevating the role of image understanding in visual question answering.
- Yash Goyal, Tejas Khot, Douglas Summers-Stay, Dhruv Batra, and Devi Parikh. 2017b. Making the v in vqa matter: Elevating the role of image understanding in visual question answering. In *Proceedings of the IEEE conference on computer vision and pattern recognition*, pages 6904–6913.
- Jack Hessel and Lillian Lee. 2020. Does my multimodal model learn cross-modal interactions? it's harder to tell than you might think! *arXiv* preprint *arXiv*:2010.06572.
- Yu Huang, Junyang Lin, Chang Zhou, Hongxia Yang, and Longbo Huang. 2022. Modality competition: What makes joint training of multi-modal network fail in deep learning?(provably). In *International conference on machine learning*, pages 9226–9259. PMLR.
- Drew A Hudson and Christopher D Manning. 2019. Gqa: A new dataset for real-world visual reasoning and compositional question answering. In *Proceedings of the IEEE/CVF conference on computer vision and pattern recognition*, pages 6700–6709.
- Aapo Hyvärinen, Jarmo Hurri, and Patrik O Hoyer. 2001. Independent component analysis. In *Natural Image Statistics: A Probabilistic Approach to Early Computational Vision*, pages 151–175. Springer.
- Junnan Li, Dongxu Li, Caiming Xiong, and Steven Hoi. 2022. Blip: Bootstrapping language-image pretraining for unified vision-language understanding and generation. In *International conference on machine learning*, pages 12888–12900. PMLR.
- Paul Pu Liang, Yun Cheng, Xiang Fan, Chun Kai Ling, Suzanne Nie, Richard Chen, Zihao Deng, Nicholas Allen, Randy Auerbach, Faisal Mahmood, et al. 2023.

- Quantifying & modeling multimodal interactions: An information decomposition framework. *Advances in Neural Information Processing Systems*, 36:27351–27393.
- Paul Pu Liang, Yiwei Lyu, Gunjan Chhablani, Nihal Jain, Zihao Deng, Xingbo Wang, Louis-Philippe Morency, and Ruslan Salakhutdinov. 2022. Multiviz: Towards visualizing and understanding multimodal models. *arXiv preprint arXiv:2207.00056*.
- Haotian Liu, Chunyuan Li, Qingyang Wu, and Yong Jae Lee. 2023. Visual instruction tuning. *Advances in neural information processing systems*, 36:34892–34916.
- Yibing Liu, Haoliang Li, Yangyang Guo, Chenqi Kong, Jing Li, and Shiqi Wang. 2022. Rethinking attention-model explainability through faithfulness violation test. In *International Conference on Machine Learning*, pages 13807–13824. PMLR.
- Scott M Lundberg and Su-In Lee. 2017. A unified approach to interpreting model predictions. *Advances in neural information processing systems*, 30.
- Yiwei Lyu, Paul Pu Liang, Zihao Deng, Ruslan Salakhutdinov, and Louis-Philippe Morency. 2022. Dime: Fine-grained interpretations of multimodal models via disentangled local explanations. In *Proceedings of the 2022 AAAI/ACM Conference on AI*, *Ethics, and Society*, pages 455–467.
- Pranava Swaroop Madhyastha, Josiah Wang, and Lucia Specia. 2018. Defoiling foiled image captions. In Proceedings of the 2018 Conference of the North American Chapter of the Association for Computational Linguistics: Human Language Technologies, Volume 2 (Short Papers), pages 433–438, New Orleans, Louisiana. Association for Computational Linguistics.
- Andrés Marafioti, Orr Zohar, Miquel Farré, Merve Noyan, Elie Bakouch, Pedro Cuenca, Cyril Zakka, Loubna Ben Allal, Anton Lozhkov, Nouamane Tazi, et al. 2025. Smolvlm: Redefining small and efficient multimodal models. *arXiv preprint arXiv:2504.05299*.
- Letitia Parcalabescu, Michele Cafagna, Lilitta Muradjan, Anette Frank, Iacer Calixto, and Albert Gatt. 2022. VALSE: A task-independent benchmark for vision and language models centered on linguistic phenomena. In *Proceedings of the 60th Annual Meeting of the Association for Computational Linguistics* (Volume 1: Long Papers), pages 8253–8280, Dublin, Ireland. Association for Computational Linguistics.
- Letitia Parcalabescu and Anette Frank. 2022. Mm-shap: A performance-agnostic metric for measuring multimodal contributions in vision and language models & tasks. *arXiv preprint arXiv:2212.08158*.
- Xiaokang Peng, Yake Wei, Andong Deng, Dong Wang, and Di Hu. 2022. Balanced multimodal learning via on-the-fly gradient modulation. In *Proceedings of*

- the IEEE/CVF conference on computer vision and pattern recognition, pages 8238–8247.
- Gabriel Peyré, Marco Cuturi, et al. 2019. Computational optimal transport: With applications to data science. *Foundations and Trends® in Machine Learning*, 11(5-6):355–607.
- Tanik Saikh, Tirthankar Ghosal, Amish Mittal, Asif Ekbal, and Pushpak Bhattacharyya. 2022. Scienceqa: A novel resource for question answering on scholarly articles. *International Journal on Digital Libraries*, 23(3):289–301.
- Ramprasaath R Selvaraju, Michael Cogswell, Abhishek Das, Ramakrishna Vedantam, Devi Parikh, and Dhruv Batra. 2017. Grad-cam: Visual explanations from deep networks via gradient-based localization. In *Proceedings of the IEEE international conference on computer vision*, pages 618–626.
- Sofia Serrano and Noah A. Smith. 2019. Is attention interpretable? In *Proceedings of the 57th Annual Meeting of the Association for Computational Linguistics*, pages 2931–2951, Florence, Italy. Association for Computational Linguistics.
- Lloyd S Shapley et al. 1953. A value for n-person games.
- Ravi Shekhar, Sandro Pezzelle, Yauhen Klimovich, Aurélie Herbelot, Moin Nabi, Enver Sangineto, and Raffaella Bernardi. 2017a. FOIL it! find one mismatch between image and language caption. In *Proceedings of the 55th Annual Meeting of the Association for Computational Linguistics (Volume 1: Long Papers)*, pages 255–265, Vancouver, Canada. Association for Computational Linguistics.
- Ravi Shekhar, Sandro Pezzelle, Yauhen Klimovich, Aurélie Herbelot, Moin Nabi, Enver Sangineto, and Raffaella Bernardi. 2017b. Foil it! find one mismatch between image and language caption. *arXiv* preprint *arXiv*:1705.01359.
- Ravi Shekhar, Ece Takmaz, Raquel Fernández, and Raffaella Bernardi. 2019. Evaluating the representational hub of language and vision models. In *Proceedings of the 13th International Conference on Computational Semantics Long Papers*, pages 211–222, Gothenburg, Sweden. Association for Computational Linguistics.
- Mong Yuan Sim, Wei Emma Zhang, Xiang Dai, and Biaoyan Fang. 2025. Can vlms actually see and read? a survey on modality collapse in vision-language models. In *Findings of the Association for Computational Linguistics: ACL 2025*, pages 24452–24470.
- Suraj Srinivas and François Fleuret. 2020. Rethinking the role of gradient-based attribution methods for model interpretability. ArXiv preprint.
- Andreas Steiner, André Susano Pinto, Michael Tschannen, Daniel Keysers, Xiao Wang, Yonatan Bitton,

- Alexey Gritsenko, Matthias Minderer, Anthony Sherbondy, Shangbang Long, et al. 2024. Paligemma 2: A family of versatile vlms for transfer. *arXiv preprint arXiv:2412.03555*.
- Alane Suhr, Stephanie Zhou, Ally Zhang, Iris Zhang, Huajun Bai, and Yoav Artzi. 2018. A corpus for reasoning about natural language grounded in photographs. *arXiv* preprint arXiv:1811.00491.
- Mukund Sundararajan, Ankur Taly, and Qiqi Yan. 2017. Axiomatic attribution for deep networks. In *International Conference on Machine Learning*, pages 3319–3328. PMLR.
- Zhanliang Wang and Kai Wang. 2025. Multishap: A shapley-based framework for explaining cross-modal interactions in multimodal ai models. *arXiv* preprint *arXiv*:2508.00576.
- Yake Wei, Ruoxuan Feng, Zihe Wang, and Di Hu. 2024. Enhancing multimodal cooperation via sample-level modality valuation. In *Proceedings of the IEEE/CVF Conference on Computer Vision and Pattern Recognition*, pages 27338–27347.
- Laura Wenderoth, Konstantin Hemker, Nikola Simidjievski, and Mateja Jamnik. 2025. Measuring crossmodal interactions in multimodal models. In *Proceedings of the AAAI Conference on Artificial Intelligence*, volume 39, pages 21501–21509.
- Sarah Wiegreffe and Yuval Pinter. 2019. Attention is not not explanation. In *Proceedings of the 2019 Conference on Empirical Methods in Natural Language Processing and the 9th International Joint Conference on Natural Language Processing (EMNLP-IJCNLP)*, pages 11–20, Hong Kong, China. Association for Computational Linguistics.
- Paul L Williams and Randall D Beer. 2010. Nonnegative decomposition of multivariate information. arXiv preprint arXiv:1004.2515.
- Yue Zhuo and Zhiqiang Ge. 2024. Ig 2: Integrated gradient on iterative gradient path for feature attribution. *IEEE Transactions on Pattern Analysis and Machine Intelligence*, 46(11):7173–7190.

Appendix A Theoretical Foundations of the IPFP Framework

A.1 Verification of Assumptions

Let \mathcal{X}_1 , \mathcal{X}_2 , \mathcal{Y} be finite sets, and let $p(x_1, y)$ and $p(x_2, y)$ denote the prescribed marginals. To ensure that the alternating KL-projection updates in the IPFP procedure are well-defined and numerically stable, we assume the following standard conditions.

Assumption .1 (Feasibility). *The marginal constraints are jointly realizable:*

$$\Delta_p := \left\{ Q \in \mathbb{R}_{\geq 0}^{|\mathcal{X}_1| \times \mathcal{X}_2| \times |\mathcal{Y}|} : \sum_{x_2} Q(x_1, x_2, y) = p(x_1, y), \ \sum_{x_1} Q(x_1, x_2, y) = p(x_2, y) \right\} \neq \emptyset.$$

This ensures that a joint distribution satisfying all marginal constraints exists, that is, the projection problem is well-defined.

Assumption .2 (Strict Positivity of the reference kernel.).

$$\tilde{Q}(x_1, x_2, y) > 0 \quad \forall (x_1, x_2, y) \in X_1 \times X_2 \times Y.$$
 (11)

This avoids divisions by zero in multiplicative updates and guarantees that the logarithm in the KL divergence is well-defined.

Assumption .3 (Full label support.).

$$p(y) > 0 \quad \forall y \in \mathcal{Y}. \tag{12}$$

This prevents degenerate label slices $Q(\cdot, \cdot|y)$ from being undefined and ensures each label participates in optimization.

Since \mathcal{X}_1 , \mathcal{X}_2 , \mathcal{Y} are finite, the probability simplex is compact, and Δ_p is nonempty, closed, and convex under Assumption .1. Together with Assumption .2, which ensures strict positivity of \tilde{Q} , the KL projection problem in Equation (7) is well-defined.

Appendix B Proofs of Theorems

Theorem 3 (Existence and Uniqueness of Q^*). The subproblem in Equation (7)

$$Q^{\star} = \arg\min_{Q \in \Delta_{n}} \mathrm{KL}(Q \parallel \tilde{Q})$$

admits a unique minimizer $Q^* \in \Delta_p$.

Proof. Since \mathcal{X}_1 , \mathcal{X}_2 , \mathcal{Y} are finite, the probability simplex is compact. Under Assumption .1, the feasible set Δ_p is nonempty, closed, and convex. By Assumption .2, $\tilde{Q}>0$, and therefore the map $Q\mapsto KL(Q\parallel \tilde{Q})$ is strictly convex in Q (Cover, 1999) and lower semicontinuous. By the Weierstrass Extreme Value Theorem, a minimizer exists, and strict convexity implies that it is unique.

The alternating updates of IPFP correspond to successive Bregman projections onto the convex sets enforcing the marginal constraints. By the Csiszár-Tusnády alternating minimization theorem (Csiszár, 1984), the iterates $Q^{(t)}$ converge to the unique minimizer Q^* , and the sequence of objective values satisfies

$$KL\left(Q^{(t)} \parallel \tilde{Q}\right) \downarrow KL\left(Q^{\star} \parallel \tilde{Q}\right).$$

That is, the KL objective is monotone nonincreasing along the iterates and converges to its optimal value. \Box

Theorem 4 (Global convergence of alternating KL-projections). Let $(Q^{(t)}, \tilde{Q}^{(t)})$ be the iterates produced by the alternating minimization (See Section 3.2). Define $F(Q, \tilde{Q}) := \mathrm{KL}(Q \parallel \tilde{Q})$. Then

$$F(Q^{(t+1)}, \tilde{Q}^{(t+1)}) \leq F(Q^{(t)}, \tilde{Q}^{(t)}) \quad \forall t,$$

and the sequence $\{F(Q^{(t)}, \tilde{Q}^{(t)})\}$ converges monotonically to a unique global minimum $F^* \geq 0$. Moreover, $Q^{(t)} \rightarrow Q^*$, where Q^* is the unique minimizer of Equation (7) and $\tilde{Q}(t) \rightarrow \tilde{Q}^*$, the corresponding projection of \tilde{Q} onto $Q_y \in \Delta_p(y)$

Proof. Each alternating step of IPFP performs an exact Bregman (KL) projection onto a closed convex constraint set. Therefore,

$$F\Big(Q^{(t+1)}, \tilde{Q}^{(t)}\Big) \; \leq \; F\Big(Q^{(t)}, \tilde{Q}^{(t)}\Big) \,, \qquad F\Big(Q^{(t+1)}, \tilde{Q}^{(t+1)}\Big) \; \leq \; F\Big(Q^{(t+1)}, \tilde{Q}^{(t)}\Big) \,,$$

and combining the inequalities yields

$$F\left(Q^{(t+1)}, \tilde{Q}^{(t+1)}\right) \leq F\left(Q^{(t)}, \tilde{Q}^{(t)}\right).$$

Since $F(Q, \tilde{Q}) \geq 0$, the sequence is bounded below and therefore convergent.

Any accumulation point must satisfy optimality with respect to both KL-projection steps. By Theorem 3, the minimizer of Equation (7) is unique, and thus the entire sequence converges to Q^* . The convergence statement follows directly from the Csiszár-Tusnády alternating minimization theorem.

Appendix C Algorithm

Algorithm 1 describes the Alternating Minimization procedure using Iterative Proportional Fitting Procedure (IPFP) in the log-domain for Sinkhorn normalization.

Appendix D Layerwise Analysis

We analyzed the layerwise analysis of various models, including the SmolVLM and LLaVa, on the ScienceQA dataset and noticed some interesting details.

D.1 LLaVa

Figure 5 (right) shows how different components of information evolve across 33 layers in the model LLaVa-7B model, highlighting the decomposition of data using the PID metrics. Redundancy (blue) peaks at the first layer and decreases quickly, suggesting early filtering of redundant information. Unique Text (orange) and Unique Image (green) remain stable across layers, with text being slightly more dominant, indicating consistent processing of both modalities. Synergy (red) fluctuates, reflecting the varying ability of the model to combine text and image information effectively at different layers. This indicates that while the model processes unique text and image data efficiently, its ability to integrate both sources fluctuates, potentially affecting performance in multimodal tasks. Overall, the model demonstrates a hierarchical approach to information processing, with challenges in maintaining balanced synergy between text and image throughout the layers.

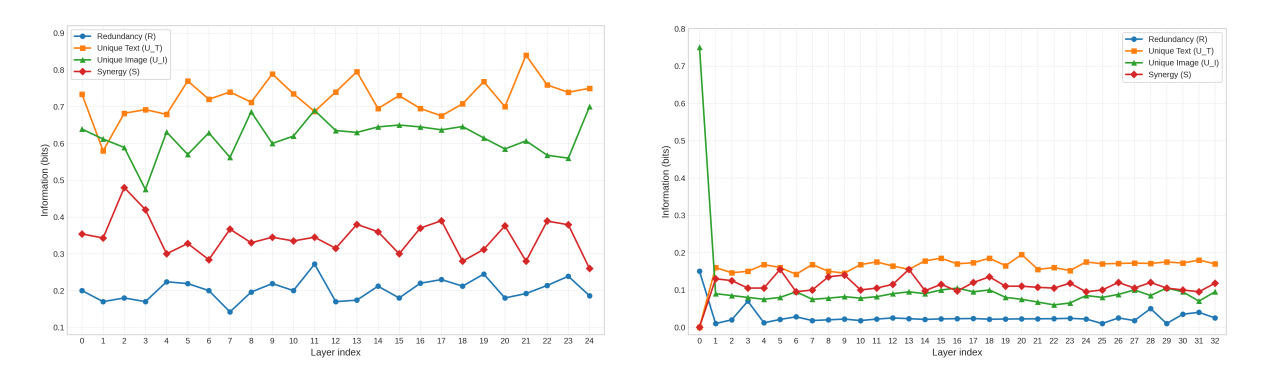


Figure 5: Layerwise analysis of SmolVLM (left) and LLaVA (right).

D.2 SmolVLM

Figure 5 (left) shows the layerwise PID decomposition for the SmolVLM model across 25 layers, breaking down information into redundancy, unique text, unique image, and synergy components. Redundancy

(blue) remains low and stable between 0.15 and 0.25 bits, indicating consistent but moderate overlapping information without a sharp initial drop. Unique Text (orange) is the dominant component, fluctuating between 0.57 and 0.85 bits, reflecting the model's strong and steady focus on extracting textual information. Unique Image (green) is also stable, ranging from 0.48 to 0.7 bits, showing consistent but somewhat lesser emphasis on image-specific information. Synergy (red) varies moderately between 0.25 and 0.48 bits, indicating ongoing but fluctuating integration of text and image information across layers. Overall, SmolVLM maintains steady redundancy, emphasizes unique text heavily, processes unique image data consistently, and exhibits moderate but variable multimodal fusion, suggesting a balanced and stable approach to multimodal understanding with a text-focused bias.

Appendix E Complexity Analysis of IPFP

Following the approach of Liang et al. (2023), the convex-programming-based estimator (CVX) computes the PID by solving a constrained convex optimization problem that maximizes the conditional entropy $\mathsf{H}_q(Y\mid X_1,X_2)$, equivalently formulated as a KL-divergence maximization over valid joint distributions $Q\in\Delta_p$ satisfying the marginal constraints. Here, $|X_1|=m$, $|X_2|=n$, and |Y|=k, so Q is a tensor of shape $m\times n\times k$. This can be cast as a conic optimization problem and solved using interior-point-based solvers such as SCS or MOSEK. Each iteration of such solvers requires matrix factorizations involving the full tensor, leading to a worst-case complexity of $\mathcal{O}((mnk)^3)$. While this approach guarantees convergence to the global optimum, the cubic dependence on the problem size makes it impractical for larger alphabets or continuous relaxations.

In contrast, our IPFP solver adopts an alternating Sinkhorn-style update scheme that enforces the marginal constraints through multiplicative scaling, avoiding expensive global factorizations. Each outer iteration updates all k conditional slices and performs approximately S inner Sinkhorn updates per slice, resulting in a per-iteration cost of $\mathcal{O}(Smnk)$ and memory complexity of $\mathcal{O}(mnk)$. In practice, the IPFP procedure converges within a few dozen iterations, achieving a near-identical solution to the CVX estimator while reducing computational cost by several orders of magnitude.

Appendix F Visualization

To qualitatively examine how the model distributes information across modalities, Table 4 visualizes several examples produced by the Paligemma-3B model on the GQA dataset. Each sample includes the input image, the corresponding question and model response, the PID metrics: redundant (**R**), unique information from text (**U1**), unique information from image (**U2**), and synergistic information (**S**), as well as the model confidence scores for the text modality (**C1**) and the image modality (**C2**).

Image	Question and Model Response	PID Metrics and Model Confidence Scores						
	User: Is it overcast? PaliGemma-3B: No	R 0.3466	U1 0.3465	U2 5 0.857	S 7 0.001	C1 0.567	C2	
	User: Who is wearing the dress? PaliGemma-3B: Woman	R 0.3635	U1 0.2772	U2 0.857	S 0.0001	C1 0.5673	C2 0.43226	
	User: Does the utensil on top of the table look clean and black? PaliGemma-3B: No	R 0.432	U1 0.399	U2 0.9464	S 0.1249	C1 0.5198	C2 0.480	
	User: Is the surfer that looks wet wearing a wetsuit? PaliGemma-3B: Yes	R 0.3696	U1 0.6308	U2 0.5241	S 0.1848	C1 0.3694	C2 0.6305	
	User: Are there clouds in the sky? PaliGemma-3B: Yes, slightly.	R 0.4123	U1 0.3521	U2	S	C1 0.592	C2	

Table 4: Examples of PID metrics and model confidence scores produced by the PaliGemma-3B model on selected samples from the GQA dataset.

```
Algorithm 1 Alternating Minimization for PID (IPFP-Based Solver)
```

```
Input: P(x_1, x_2, y); p(x_1, y), p(x_2, y); p(y)
                                                                                                     ⊳ joint empirical + marginals
Hyperparameters: T, S, \tau_{\text{outer}}, \tau_{\text{sink}}, \varepsilon > 0
Output: Q^*, R, U_1, U_2, S, C_1, C_2,
  1: Define feasible set \Delta_p (Eq. (5)) and objective (Eq. (7))

⊳ KL-projection problem

 2: Initialization: For each y
                                          Q^{(0)}(\cdot,\cdot,y) = \max\left(\frac{p(x_1,y)\,p(x_2,y)^{\top}}{p(y)},\,\varepsilon\right)
                                     Q^{(0)}(\cdot,\cdot,y) \leftarrow Q^{(0)}(\cdot,\cdot,y) \cdot \frac{p(y)}{\sum_{x_1,x_2} Q^{(0)}(x_1,x_2,y)}
                                                                                               ▷ label-wise product initialization
 3: for t = 0 to T - 1 do
          \tilde{Q}^{(t)}(x_1, x_2, y) = Q^{(t)}(x_1, x_2)/|\mathcal{Y}|
 4:
                                                                                                        ⊳ auxiliary update (Eq. (6))
          for each y with p(y) > \varepsilon do
 5:
                A_y \leftarrow \tilde{Q}^{(t)}(\cdot,\cdot,y)
 6:
                                                                                                                \log r_y = \log(\max(p(x_1, y), \varepsilon)); \log c_y = \log(\max(p(x_2, y), \varepsilon))
                                                                                                               > stabilized marginals
 7:
 8:
                     \log u_y \leftarrow \log r_y - LSE_{x_2}(\log A_y + \log v_y)
 9:
                    \log v_y^{\text{new}} \leftarrow \log c_y - \text{LSE}_{x_1}(\log A_y + \log u_y)
10:
               \log v_y \leftarrow \log v_y^{\text{new}}
until \|\log v_y^{\text{new}} - \log v_y\|_{\infty} < \tau_{\text{sink}}
11:
12:
                                                                                     ▷ log-domain Sinkhorn updates (Eq. (8))
               Q^{(t+1)}(\cdot,\cdot,y) = \exp(\log A_y + \log u_y + \log v_y)
13:
                                                                                                ⊳ recover transport plan (Eq. (9))
               Q^{(t+1)} \leftarrow \max(Q^{(t+1)}, \varepsilon)
                                                                                                                     ▷ numerical floor
14:
               Normalize \sum_{x_1,x_2} Q^{(t+1)}(\cdot,\cdot,y) = p(y)
15:
                                                                                                                  ⊳ mass-fix per label
16:
          end for
          F^{(t+1)} = \mathrm{KL}(Q^{(t+1)} || \tilde{Q}^{(t)})
                                                                                                                 ⊳ evaluate objective
17:
          if \frac{|F^{(t+1)}-F^{(t)}|}{\max(1,|F^{(t)}|)} < 	au_{\text{outer}} then
                                                                                                     ▷ relative improvement small
18:
19:
               break
20:
          end if
21: end for
22: Q^* \leftarrow Q^{(t+1)}
                                                                                                                       23: Compute R, U_1, U_2, S via Eqs. (1)-(4)
                                                                                                                   ▶ PID components
24: C_1 = U_1/(U_1 + U_2), C_2 = U_2/(U_1 + U_2)
                                                                             ⊳ normalized modality contributions (Eq. (10))
25: return Q^*, R, U_1, U_2, S, C_1, C_2
```